

Topological junctions in high-Chern-number quantum anomalous Hall systems


Yulei Han¹, Shiyao Pan¹ and Zhenhua Qiao^{2,3,*}

¹*Department of Physics, Fuzhou University, Fuzhou, Fujian 350108, China*

²*International Centre for Quantum Design of Functional Materials, CAS Key Laboratory of Strongly-Coupled Quantum Matter Physics, and*

Department of Physics, University of Science and Technology of China, Hefei, Anhui 230026, China

³*Hefei National Laboratory, University of Science and Technology of China, Hefei 230088, China*

 (Received 19 April 2023; revised 4 August 2023; accepted 21 August 2023; published 5 September 2023)

Quantum anomalous Hall effect (QAHE) is the real topological state without magnetic field that is robust against any perturbations, and is related to a bulk topological number \mathcal{C} , counting the number of chiral edge modes. Such chiral edge modes also exist at the magnetic domain walls between regions with different Chern numbers. Here, we systematically investigate the electronic properties of topological junctions formed at boundaries of QAHEs with different Chern numbers. We find that the number of chiral edge modes along the junction is determined by the difference of Chern numbers of adjacent regions, which can be understood from the coupling between counterpropagating channels along the junction. Finally, we show that the current partition of topological junctions can be flexibly manipulated by tuning the number of quantum anomalous Hall regions, Chern numbers, and the magnetization directions. Our work provides an ideal platform to design multichannel low-power devices for electronic circuits and switching applications.

DOI: [10.1103/PhysRevB.108.115302](https://doi.org/10.1103/PhysRevB.108.115302)

I. INTRODUCTION

Quantum anomalous Hall effect (QAHE) is a topological phase of matter characterized by quantized Hall conductance and vanishing longitudinal resistance in the absence of external magnetic field [1–5]. The bulk is insulating and the corresponding system boundaries carry conducting chiral edge states. Its nontrivial topology is closely related to a topological invariant, i.e., Chern number \mathcal{C} [6]. Due to the bulk-boundary correspondence, the Chern number can be directly associated with the number of chiral edge states and the quantized Hall conductance of $\mathcal{C}e^2/h$. Like the traditional QHE, QAHE is robust against any kind of disorders, and therefore is the most ideal materials for potential applications in low-power electronic devices [5].

In 1988, Haldane first proposed the QAHE in a honeycomb lattice model, which was once considered to be a toy system [1]. Little progress was made till the first experimental discovery of monolayer graphene in 2004. Since then, QAHE has been becoming a seminal hot topic, which is still attracting more focus from different research fields. Several representative theoretical proposals are made in various two-dimensional materials [7–18], among which the $\mathcal{C} = 1$ QAHE was first experimentally observed in magnetically doped topological insulator thin films [19–21] and then in intrinsic magnetic topological insulator MnBi_2Te_4 [22], moiré bilayer graphene systems [23], and transition-metal dichalcogenides [24]. Based on $\mathcal{C} = 1$ QAHE systems, one-dimensional chiral conducting states can be produced along the magnetic domain walls formed between QAHEs with opposite Chern numbers

[25–29], making them suitable for designing programmable integrated circuits [30] and topological networks [27,31].

Besides the $\mathcal{C} = 1$ QAHE, high-Chern-number QAHE is highly desired because of their multiple chiral edge channels, which can significantly improve the performance of QAHE devices and facilitate potential applications in multichannel quantum computing [32]. QAHE with high Chern number was proposed in multilayer of magnetic topological insulators [33,34] and thin films of topological crystalline insulators [11]. Recently, it was demonstrated that high-Chern-number QAH effect can be realized in MnBi_2Te_4 multilayer with $\mathcal{C} = 2$ [35–38] and monolayer transitional-metal oxides with $\mathcal{C} = 3$ [39]. Besides the intrinsic materials, van der Waals stacking of two-dimensional materials is also an important approach to achieve high-Chern-number QAH effect [33,40–43], such as in trilayer graphene/ h -BN moiré superlattice with $\mathcal{C} = 2$ [40], and in magnetic topological insulator-based multilayer structures with tunable Chern number [33,41–43]. Recently, the topological junction formed by QAHEs with different Chern numbers can be experimentally fabricated, and a unique chiral edge mode along the junction interface has been identified in MnBi_2Te_4 [44] and Cr-doped $(\text{Bi}, \text{Sb})_2\text{Te}_3/(\text{Bi}, \text{Sb})_2\text{Te}_3$ multilayers [45], which can be used to construct topological circuits by controlling the Chern numbers of each domain. However, the underlying physical mechanism remains unclear, hindering its potential applications. In addition, the fractional Hall conductance was observed in graphene p - n quantum Hall junctions, where the regions with different Chern numbers modulated by tuning the carrier densities [46,47]. However, the band structures associated with the quantum Hall effect and QAH effect are distinct, i.e., Landau levels in quantum Hall effect whereas inverted bands in QAHE, leading to different band origins of topological states.

*Corresponding author: qiao@ustc.edu.cn

In this work, we reveal the physical origin of the unique chiral edge mode in the topological junctions by utilizing model analysis and electronic transport calculations. In a two-domain topological junction with arbitrary Chern numbers, we find that the current distributions along the junction interface are determined by the Chern numbers of individual regions, i.e., the number of gapless modes along the junction interface is proportional to the Chern number difference of the two domains. To fully understand the underlying physical mechanism, we construct an effective model and find the crucial role of coupling between counterpropagating channels in determining the number of gapless states along the junction interface. We also show that the number of conducting channels and the current propagating directions along the junction interface can be controlled by manipulating the number of QAHE domains, Chern numbers, and magnetization directions of each domain.

II. HAMILTONIAN AND METHODS

To explore the electronic and topological properties of high-Chern-number QAH junctions, we take magnetically doped topological insulator thin films as our model systems. The tight-binding model Hamiltonian can be written as [34,48]

$$H = \sum_{\alpha,i} c_{i+1}^\dagger T_\alpha c_i + \sum_{i \in \mathcal{R}} [E_0(\mathcal{R}) + m(\mathcal{R})] c_i^\dagger c_i + \text{H.c.}, \quad (1)$$

where $T_\alpha = B\sigma_z \otimes s_0 + \frac{iA}{2}\sigma_x \otimes s_\alpha$ with $\alpha = x, y, z$, $E_0(\mathcal{R}) = [M_0(\mathcal{R}) - 6B]\sigma_z \otimes s_0$, and $m(\mathcal{R}) = g(\mathcal{R})\sigma_0 \otimes s_z$. σ and s are Pauli matrices for the orbital and spin degrees of freedom, respectively. The first term represents the electron hopping, whereas the second term denotes the on-site energy applied to domain \mathcal{R} with \mathcal{R} denoting the individual domains of the topological junction. M_0 characterizes the band inversion strength and g represents the ferromagnetic strength. The thin film thickness is along z direction, with N_z representing the layer number. Without loss of generality, hereinbelow we set $A = 1.0$, $B = 0.7$, and $M_0 = 0.5$.

The topological properties of the system are determined by calculating the momentum-space Berry curvature [6,8]:

$$\Omega_n(\mathbf{k}) = - \sum_{m \neq n} \frac{2\text{Im} \langle \psi_{n\mathbf{k}} | v_x | \psi_{m\mathbf{k}} \rangle \langle \psi_{m\mathbf{k}} | v_y | \psi_{n\mathbf{k}} \rangle}{(E_m - E_n)^2}, \quad (2)$$

where E_n and $\psi_{n\mathbf{k}}$ are the eigenvalue and eigenstate of the n th band, respectively. $v_{x/y} = \frac{1}{\hbar} \frac{\partial E(k)}{\partial k_{x/y}}$ stands for velocity operator along the x/y direction. The Chern number of the system can be calculated by $\mathcal{C} = \frac{1}{2\pi} \sum_n \int_{\text{BZ}} d^2k \Omega_n$, where the summation is over all occupied bands and the integration is over the first Brillouin zone.

The multiterminal electronic transport properties of the system are evaluated by the Landauer-Büttiker formula, and the conductance from lead p to lead q can be written as [49]:

$$G_{pq} = \left(\frac{e^2}{h} \right) \text{Tr}(\Gamma_q G^r \Gamma_p G^a), \quad (3)$$

where $G^{r/a}$ is the retarded/advanced Green's function of the central scattering region, $\Gamma_p = i(\sum_p^r - \sum_p^a)$ is the line-width function coupling lead p to the central scattering region, and

$\sum_p^{r/a}$ is the retarded/advanced self-energy of the semi-infinite lead p that can be obtained by using the variant transfer matrix method [50]. The real-space local density of states of the central scattering region for electrons injected from lead p can be evaluated by $\rho_p(\mathbf{r}, \epsilon) = \frac{1}{2\pi} G^r \Gamma_p G^a$, where \mathbf{r} is the real-space coordinate and ϵ is the Fermi level.

III. ELECTRONIC PROPERTIES OF TOPOLOGICAL JUNCTIONS

To illustrate the electronic properties of topological junctions with two domains ($\mathcal{R} = 1, 2$), we begin with the $\mathcal{C}_{\text{max}} = 2$ case and use $g = 1.4$ (2.5) to simulate $\mathcal{C} = 1$ (2) QAHE with $N_z = 2$. In $\mathcal{C}_{\text{max}} = 2$ situation, each region of the junction has four possible nonzero Chern numbers, i.e., $\mathcal{C}_{\mathcal{R}} = \pm 1, \pm 2$, yielding two distinct types of combinations, i.e., (i) $|\mathcal{C}_1| = |\mathcal{C}_2|$, and (ii) $|\mathcal{C}_1| \neq |\mathcal{C}_2|$. For $|\mathcal{C}_1| = |\mathcal{C}_2|$, there are two different combinations, i.e., $\mathcal{C}_1 = \mathcal{C}_2$ and $\mathcal{C}_1 = -\mathcal{C}_2$. When $\mathcal{C}_1 = \mathcal{C}_2$, the topological junction can be considered as a homogeneous QAHE without domain wall, implying that chiral gapless states exist simply along the sample edges. When $\mathcal{C}_1 = -\mathcal{C}_2$ (see Appendix A), the presence of domain wall can induce one-dimensional topological conducting channels along the junction interface, as previously predicted [27].

For $|\mathcal{C}_1| \neq |\mathcal{C}_2|$, there are two independent cases of combinations, i.e., $(\mathcal{C}_1, \mathcal{C}_2) = (1, 2)$ and $(1, -2)$. When $(\mathcal{C}_1, \mathcal{C}_2) = (1, 2)$, the schematic plot of topological junction is displayed in Fig. 1(a), which has recently been experimentally fabricated [44,45]. One can find the counterpropagating doubly degenerated gapless states labeled by red and blue in Fig. 1(b). As shown in Fig. 1(c), the gapless states are distributed in different regions, with the two blue gapless states propagating along the $-x$ direction separately distributed in

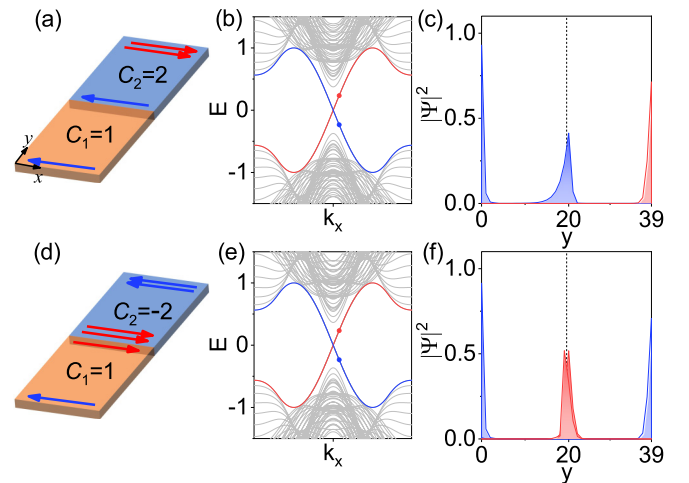


FIG. 1. Electronic properties of topological junctions with two domains exhibiting different Chern numbers. (a) Schematic plot of a topological junction with $(\mathcal{C}_1, \mathcal{C}_2) = (1, 2)$, (b) the corresponding one-dimensional electronic band structures, and (c) wave function distributions of the gapless states along the y direction of the junction. (d)–(f) For a topological junction with $(\mathcal{C}_1, \mathcal{C}_2) = (1, -2)$. The red (blue) arrows represent the gapless states propagating along x ($-x$) direction. The black dashed lines in (c) and (f) represent the junction interface.

the lower sample edge and the junction interface, and the doubly degenerated red gapless states propagating along the x direction located in the upper sample edge. These gapless states are clearly illustrated by blue and red arrows in Fig. 1(a). It is noteworthy that the numbers and distributions of gapless states in the topological junction are consistent with the experimental observations [44,45], indicating that our theoretical models are valid.

When $(C_1, C_2) = (1, -2)$, the gapless states are triply degenerated, with three propagating along the x direction of the junction interface and three propagating along the $-x$ direction of the sample edges, as shown in Figs. 1(d)–1(f). It should be noted that the total number of conducting channels along the junction interface equals to $|C_1 - C_2|$. Furthermore, unlike electric-gating-controlled topological conducting states in graphene with a fixed number of channels [51–53], the number of conducting channels in QAHE junctions can be flexibly tuned by adjusting the Chern number of individual regions.

IV. ORIGIN OF NUMBER OF GAPLESS MODES ALONG JUNCTION INTERFACE

In a topological junction, one can categorize the gapless states into two types based on their distribution, with one type being located at the sample edges and the other type being located at the junction interface. The number of chiral edge states of QAHE is definitely determined by the Chern number $C_{\mathcal{R}}$, due to the bulk-boundary correspondence. However, the number of gapless states along the junction interface is determined by the difference between the Chern numbers of the two regions, i.e., $|C_1 - C_2|$.

To better understand the one-dimensional band structure of the gapless states along the junction interface, we construct an effective model on the basis of chiral edge channels confined in the junction interface. The general Hamiltonian can be written as [54,55]:

$$H(k_x) = \begin{pmatrix} \hbar v_F k_x & \delta & 0 & 0 & & \\ \delta & -\hbar v_F k_x & \delta & 0 & \dots & \dots \\ 0 & \delta & \hbar v_F k_x & \delta & \dots & \dots \\ 0 & 0 & \delta & -\hbar v_F k_x & & \\ & \vdots & \vdots & & & \\ & \vdots & \vdots & & & \end{pmatrix}, \quad (4)$$

where $\pm \hbar v_F k$ represent the kinetic energy of each channel propagating along $\pm x$ of the junction interface. δ describes the coupling strength between counterpropagating channels and is proportional to \exp^{-d} where d measures the distance between the two domains. The matrix dimension is determined by the sum of Chern values of individual regions, i.e., $|C_1| + |C_2|$. In general, the solution of the matrix is determined by the Chern number of each domain. Thus, the analytical diagonalization of the high-dimensional matrix is extremely difficult. Below, we demonstrate two cases to illustrate the validness of the effective model and the crucial role of coupling between counterpropagating channels.

For sake of clarity, we first consider a $C = 1$ QAHE, which can also be viewed as a topological junction with $C_1 = 1$ and

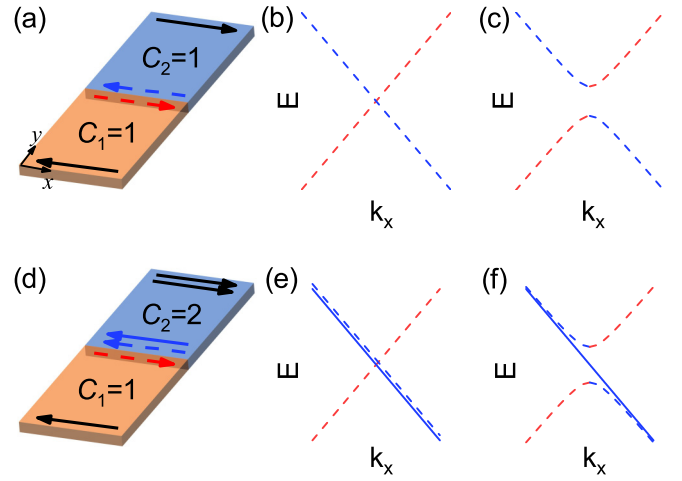


FIG. 2. (a) Schematic plot of a topological junction with $(C_1, C_2) = (1, 1)$. (b)–(c): The one-dimensional electronic band structures along the junction interface (b) without and (c) with coupling between counterpropagating channels, respectively. (d)–(f) For a topological junction with $(C_1, C_2) = (1, 2)$. The red (blue) arrows represent the gapless states propagating along the x ($-x$) direction of the junction interface. The black arrows represent the edge states.

$C_2 = 1$, as demonstrated in Fig. 2(a). The gapless states of the system should be absent along the junction interface and only present along the sample edges [see black arrows in Fig. 2(a)]. Nonetheless, we can still define a pair of virtual counterpropagating channels along the junction interface [see blue and red arrows in Fig. 2(a)], assuming decoupling between the two $C = 1$ QAHEs. Now, the effective matrix can be written as

$$H(k_x) = \begin{pmatrix} \hbar v_F k_x & \delta \\ \delta & -\hbar v_F k_x \end{pmatrix}. \quad (5)$$

One can obtain the eigenvalues as $E_{\pm} = \pm \sqrt{(\hbar v_F k_x)^2 + \delta^2}$. For $\delta = 0$, $E_{\pm} = \pm \hbar v_F k_x$, and the corresponding band structure is displayed in Fig. 2(b), indicating that decoupling between the two $C = 1$ QAHE domains leads to two gapless states along the interface. For $\delta \neq 0$, a band gap of 2δ opens, resulting in the absence of gapless states along the junction interface [see Fig. 2(c)]. As a consequence, the gapless states only exist at sample boundaries [26].

We then consider a topological junction with $C_1 = 1$ and $C_2 = 2$, as displayed in Fig. 2(d). When the two domains are decoupled, there should be one channel propagating along x direction and two channels propagating along $-x$ direction of the junction interface [see blue and red arrows in Fig. 2(d)]. The effective matrix can be written as

$$H(k_x) = \begin{pmatrix} -\hbar v_F k_x & \delta & 0 \\ \delta & \hbar v_F k_x & \delta \\ 0 & \delta & -\hbar v_F k_x \end{pmatrix}, \quad (6)$$

The eigenvalues are $E_{1\pm} = \pm \sqrt{(\hbar v_F k_x)^2 + 2\delta^2}$, $E_2 = -\hbar v_F k_x$. For $\delta = 0$, the eigenvalues are $E_{1+} = \hbar v_F k_x$ and $E_{1-} = E_2 = -\hbar v_F k_x$, and the corresponding band structure is displayed in Fig. 2(e). For $\delta \neq 0$, a local gap of $\sqrt{2}\delta$ between E_{1+} and E_{1-} at $k_x = 0$ opens, whereas the gapless state $E_2 = -\hbar v_F k_x$ remains unchanged, as displayed in Fig. 2(f). Consequently, only one gapless state along the

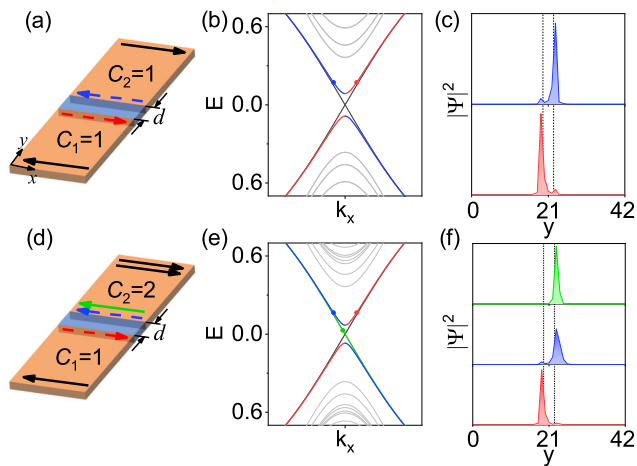


FIG. 3. (a) Schematic plot of a topological junction with $(C_1, C_2) = (1, 1)$. The orange (blue) regions represent QAH (normal) insulator, and the distance between the two QAH insulator regions is denoted by d ($d = 3$). (b) The one-dimensional electronic band structures, and (c) the wave-function distributions of electronic states around the junction interface. (d) Schematic plot of a topological junction with $(C_1, C_2) = (1, 2)$. (e) The one-dimensional electronic band structures, and (f) the wave-function distributions of electronic states around the junction interface. The red (blue or green) colors represent the interfacial states propagating along the x ($-x$) direction of the junction interface. The black dashed lines in (c) and (f) represent the junction interface.

junction interface survives, as shown by the solid blue arrow in Fig. 2(d). For arbitrary C_1 and C_2 , this effective model can perfectly capture the low-energy physics of the band structures along the interface of topological junctions, implying the crucial role of coupling between counterpropagating channels along the junction interface.

It is worth noting that in a topological junction the strength of δ decreases exponentially as the distance d between the two domains increases. In Fig. 1(a), the two directly connected QAH regions of the topological junction result in $d = 0$ and the maximum value of δ . Therefore, the δ -induced local gap cannot be observed clearly in Fig. 1(b), since the large δ -induced local gap exceeds the bulk band gap of the system.

In order to clearly demonstrate the δ -induced local gap from the tight-binding model, we can construct a topological junction with a nonzero d , i.e., two QAH regions connected by a normal insulator region. The presence of a nonzero d suggests a weak coupling between counterpropagating channels along the junction interface, resulting in a visible δ -induced local gap that is smaller than the bulk gap. As displayed in Fig. 3(a), the topological junction is composed of two $C = 1$ QAH regions joined by a $d = 3$ normal insulator. One can clearly observe the δ -induced local gap in Fig. 3(b), which is depicted by red and blue colors, and the wave-function distributions in Fig. 3(c) demonstrate that the red and blue states are primarily confined to the interfacial QAH regions, with a slight mixing of states. Similarly, when $(C_1, C_2) = (1, 2)$, the topological junction is illustrated in Fig. 3(d). Besides the coupling between counterpropagating channels induced gapless states along the junction interface, we can clearly

see the gapped channels labeled by red and blue along the interfacial QAH regions in Figs. 3(e)–3(f). Therefore, by combining the effective model and the tight-binding Hamiltonian, we explicitly reveal the essential role of coupling between counterpropagating channels in determining the number of gapless states along the QAH junction interface.

V. CURRENT PARTITIONS AT TOPOLOGICAL JUNCTIONS

To directly reveal the intriguing electronic properties of topological junctions, we study the transport properties of the two-domain topological junctions. To ensure the existence of gapless states along the junction interface, i.e. $C_1 \neq C_2$, we consider four combinations of (C_1, C_2) : $(1, 2)$, $(-1, -2)$, $(1, -2)$, and $(-1, 2)$. We then construct topological junctions with four leads labeled as 1–4, as displayed in Fig. 4. The corresponding four-terminal conductances as a function of the Fermi level are presented in Figs. 10–13 (see Appendix B), respectively. When the Fermi level is in the bulk band gap, the four-terminal conductances are either quantized or vanishing. Therefore, we focus on the current partitions of the topological junctions.

Figures 4(a)–4(d) display the local density of states of the topological junction with $(C_1, C_2) = (1, 2)$ for electrons injected from leads 1–4, respectively. Due to the presence of one conducting channel propagating along the left direction of the junction interface, the electrons injected from lead 1 can only transmit to lead 2 with a quantized conductance of e^2/h , as shown in Fig. 4(a), whereas the electrons injected from lead 3 become split into two parts at the junction interface and finally transport into leads 2 and 4, respectively, as displayed in Fig. 4(c). The conductance and current direction in the bottom/top boundary of the system are determined by the value and the sign of the Chern number of each domain. Specifically, the electrons injected from lead 2 transmit to lead 3 along the top boundary with a quantized conductance of $2e^2/h$, as shown Fig. 4(b), while the electrons injected from

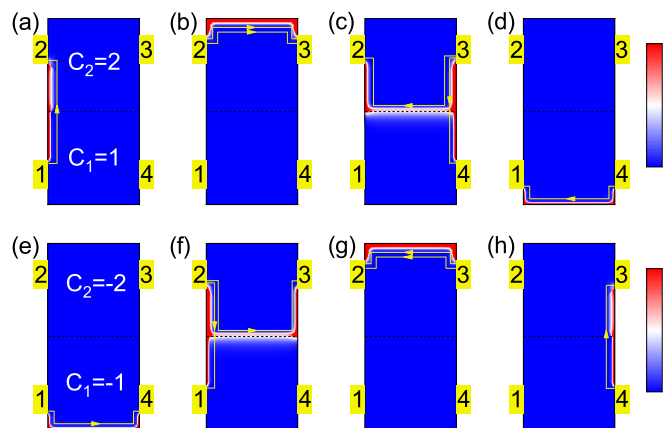


FIG. 4. (a)–(d) Local density of states of topological junctions with $(C_1, C_2) = (1, 2)$ for electrons injected from lead 1 to lead 4, respectively. (e)–(f) For a topological junction with $(C_1, C_2) = (-1, -2)$. The color bar represents the density of electrons. The yellow arrows represent the current flow. The Fermi level is set to be $E_F = 0.01$ and the length of each region is 30 lattice sites.

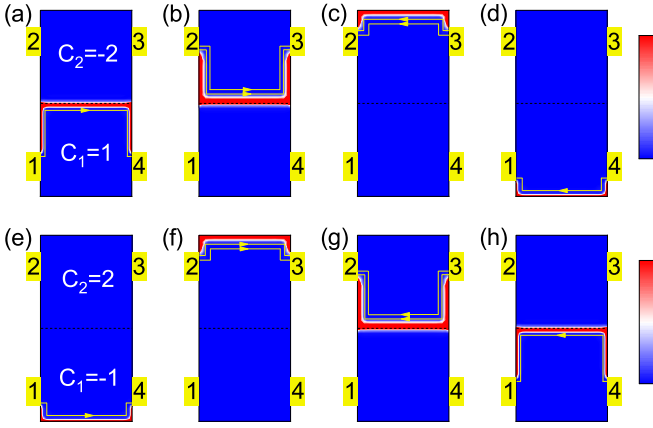


FIG. 5. (a)–(d) Local density of states of topological junctions with $(C_1, C_2) = (1, -2)$ for electrons injected from lead 1 to lead 4, respectively. (e)–(f) For a topological junction with $(C_1, C_2) = (-1, 2)$. The color bar represents the density of electrons. The yellow arrows represent the current flow. The Fermi level is set to be $E_F = 0.01$ and the length of each region is 30 lattice sites.

lead 4 transmit to lead 1 along the bottom boundary with a quantized conductance of e^2/h , as demonstrated in Fig. 4(d).

When the magnetization direction is flipped, the Chern numbers change to $(C_1, C_2) = (-1, -2)$, and the corresponding local density of states are demonstrated in Figs. 4(e)–4(f). The conducting channel along the junction interface now reverses its propagating direction to the right side, resulting in different current partition forms. Unlike the above case with positive Chern numbers, the electrons injected from lead 1 (3) now transmit through the bottom (top) boundary to lead 4 (2) with quantized conductance of e^2/h ($2e^2/h$), as shown in Figs. 4(e) and 4(g), respectively. Meanwhile, the electrons injected from lead 2 become split into two parts at the junction

interface and finally transport into leads 1 and 3, respectively, as shown in Fig. 4(f). The electrons injected from lead 4 only transmit to lead 3 with a quantized conductance of e^2/h [see Fig. 4(h)]. Recently, the above configurations have been experimentally measured [44]. Our theoretical calculations provide a deep understanding of the underlying physics of the topological junction, as well as a thorough explanation of the experimental observations.

We then study the electronic transport properties of topological junction with $(C_1, C_2) = (1, -2)$, as displayed in Figs. 5(a)–5(d). In this case, three electronic channels are propagating along the right side of the junction interface. One of the channels is contributed by region \mathcal{R}_1 , while the other two are contributed by region \mathcal{R}_2 . As displayed in Fig. 5(a), the electrons injected from lead 1 directly transmit to lead 4 along the junction interface with a quantized conductance of e^2/h . Similarly, the electrons injected from lead 2 transmit straight to lead 3 along the junction interface a quantized conductance of $2e^2/h$, as shown in Fig. 5(b). The electrons injected from lead 3 (4) transmit along the top (bottom) boundary, as displayed in Figs. 5(c) and 5(d), respectively. When the magnetization direction is reversed, the Chern number changes to $(C_1, C_2) = (-1, 2)$, and the electron loops in each region reverse transport directions, as demonstrated in Figs. 5(e)–5(h).

To clearly show the move direction of electrons in topological junctions with different combinations of Chern numbers, we show the schematic plot of the current flow in Fig. 6. The transport results presented above demonstrate that coupling of interfacial channels occurs only between counterpropagating channels along the junction interface, i.e., $C_1 \cdot C_2 > 0$; whereas the two regions of the junction are decoupled when the interfacial channels in the two regions propagate in the same direction, i.e., $C_1 \cdot C_2 < 0$. Therefore, the current partition of the topological junction can be tuned feasibly by adjusting the Chern numbers or the magnetization directions of individual regions.

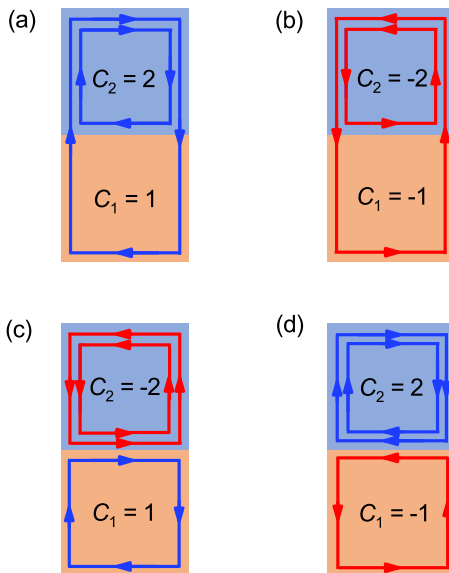


FIG. 6. The schematic plot of the current flow in the two-region topological junctions. The red (blue) color represents the anticlockwise (clockwise) loop.

VI. TOPOLOGICAL JUNCTIONS WITH HIGHER CHERN NUMBERS AND MORE DOMAINS

We then demonstrate how the above conclusion can be extended to systems with higher Chern numbers and more domains. In a two-domain topological junction with higher Chern numbers, Figure 7 displays the four-terminal conductance inside the bulk gap in the (C_1, C_2) space, where C_1 and C_2 vary from -4 to 4 . From the discussion in the previous section, we know that the current partitions between G_{12} and G_{34} are different. However, we can observe that G_{12} and G_{34} have the same distributions in (C_1, C_2) space, and both are nonzero only when $C_1, C_2 > 0$. For instance, when $C_2 > C_1 > 0$, the conductance G_{12} is equal to $C_1 e^2/h$, whereas G_{32} flowing through the junction interface should be $(C_2 - C_1) e^2/h$, resulting in the conductance G_{34} being $C_2 e^2/h - G_{32} = C_1 e^2/h$. When the magnetization direction changes, the chirality (electron flow direction) also reverses, causing G_{pq} and G_{qp} to be symmetric about the phase space center $(C_1, C_2) = (0, 0)$. Based on this variation pattern, the four-terminal conductance diagram can be further extended to situations with higher Chern numbers.

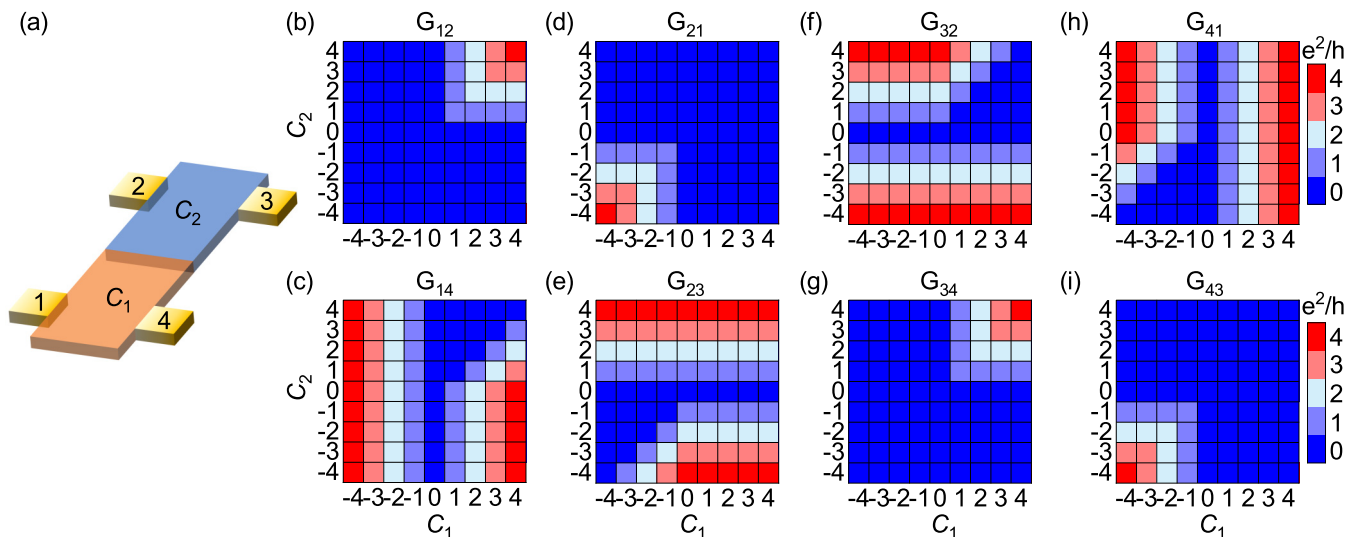


FIG. 7. (a) Schematic plot of a four-terminal transport device with two domains. (b)–(i) The conductance G_{pq} from lead p to lead q inside the bulk gap with $p, q = 1-4$ in the (C_1, C_2) space. The color bar represents the quantized value of conductance in unit of e^2/h . The G_{13}, G_{24}, G_{31} , and G_{42} are all zero in the (C_1, C_2) space and do not show here.

We explore the influence of the number of domains on the electronic distributions of topological junctions. In order to induce coupling between counterpropagating chan-

nels along the junction interfaces, we assume that the Chern numbers of individual domains are all positive. Figure 8 displays three typical three-domain topological junctions with distinct electronic distributions, each containing two junction interfaces. When $C_2 > C_1$ and $C_2 > C_3$, as displayed in Figs. 8(a)–8(c) for $(C_1, C_2, C_3) = (1, 2, 1)$, a gapless state propagates along $-x$ direction of the first junction interface ($y \approx 20$), while another gapless state propagates along x direction of the second junction interface ($y \approx 40$). Conversely, when $C_2 < C_1$ and $C_2 < C_3$, as displayed in Figs. 8(d)–8(f) for $(C_1, C_2, C_3) = (2, 1, 2)$, the propagating directions of the

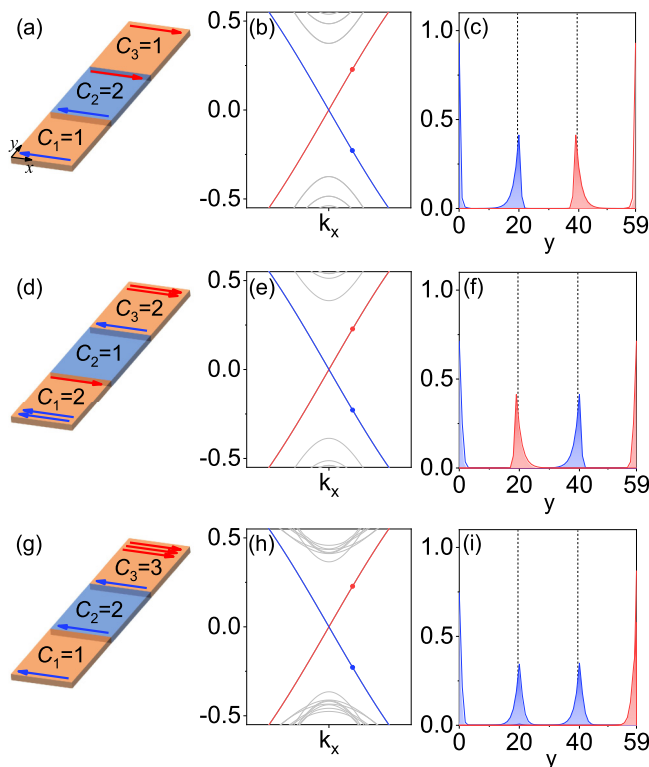


FIG. 8. Electronic properties of topological junctions with three domains. (a) Schematic plot of a topological junction with $(C_1, C_2, C_3) = (1, 2, 1)$, (b) the corresponding one-dimensional electronic band structures, and (c) wave function distributions of the gapless states along the y direction. (d)–(f) For a system with $(C_1, C_2, C_3) = (2, 1, 2)$. (g)–(i) For a system with $(C_1, C_2, C_3) = (1, 2, 3)$. The red (blue) arrows represent the gapless states propagating along the x ($-x$) direction. The black dashed lines in (c), (f), and (i) represent the junction interface.

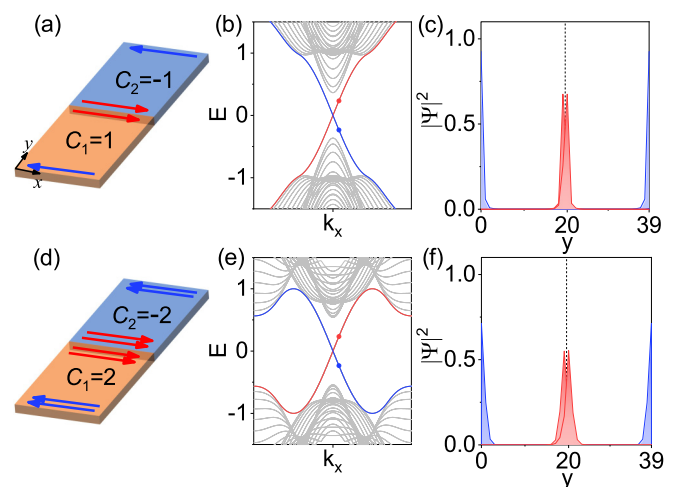


FIG. 9. Electronic properties of topological junctions with two domains harboring opposite Chern numbers. (a) Schematic plot of a topological junction with $C_1 = -C_2 = 1$, (b) the corresponding one-dimensional electronic band structures, and (c) wave-function distributions of the gapless states along the y direction of the junction. (d)–(f) For a topological junction with $C_1 = -C_2 = 2$. The red (blue) arrows represent the gapless states propagating along the x ($-x$) direction. The black dashed lines in (c) and (f) represent the junction interface.

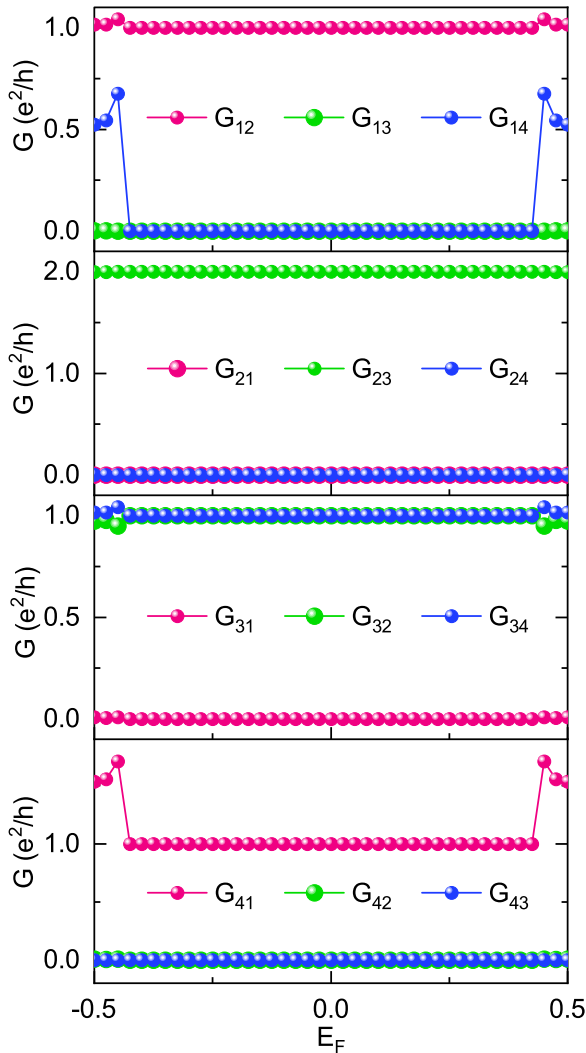


FIG. 10. The four-terminal conductance of the two-region topological junction with $(C_1, C_2) = (1, 2)$ as a function of Fermi level E_F .

gapless states in the two junction interfaces become reversed. When $C_2 > C_1$ and $C_2 < C_3$, as depicted in Figs. 8(g)–8(i) for $(C_1, C_2, C_3) = (1, 2, 3)$, the gapless states in both junction interfaces propagate along $-x$ direction. Thus, the conclusion drawn from the two-domain topological junction can be directly extended to systems with higher Chern numbers and more QAHE domains. Moreover, the number of QAHE domains is a crucial factor in tuning current partitions of the topological junctions.

VII. SUMMARY

We comprehensively investigated the electronic properties of topological junctions in high-Chern-number quantum anomalous Hall systems. Our results demonstrate that the choice of Chern number of individual domains is crucial in determining the intriguing electronic distributions along the junction interface. Specifically, the number of topological gapless states along the junction interface is determined by the Chern number difference of the two domains, i.e., $|C_1 - C_2|$,

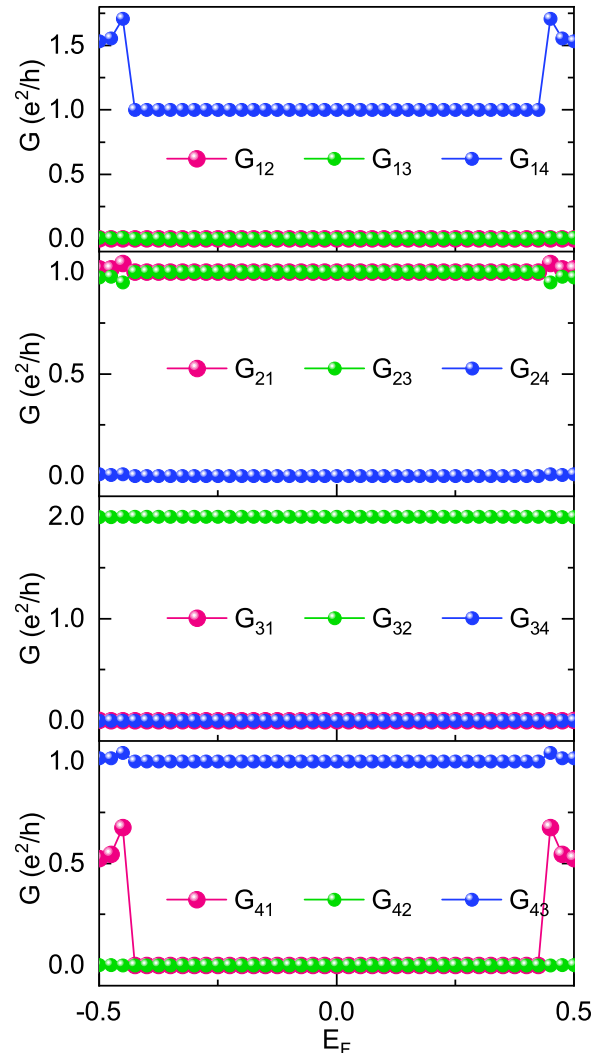


FIG. 11. The four-terminal conductance of the two-region topological junction with $(C_1, C_2) = (-1, -2)$ as a function of Fermi level E_F .

which is further elucidated by an effective model. Our findings also highlight the crucial role of coupling between counter-propagating channels in determining the number of gapless states along the junction interface. Furthermore, we show that the number of channels and the propagating direction of electrons along the junction interface can be flexibly controlled by varying the number of quantum anomalous Hall domains, Chern numbers, or the magnetization directions of individual regions. Our work elucidates the physical origin of the existence of topological chiral edge states along the QAHE junction interface, which could facilitate the potential applications of multichannel topological circuits, switching devices, and chiral interconnects.

ACKNOWLEDGMENTS

This work was financially supported by the National Natural Science Foundation of China (Grants No. 12004369 and No. 11974327), Natural Science Foundation of Fujian Province (No. 2022J05019), Fundamental

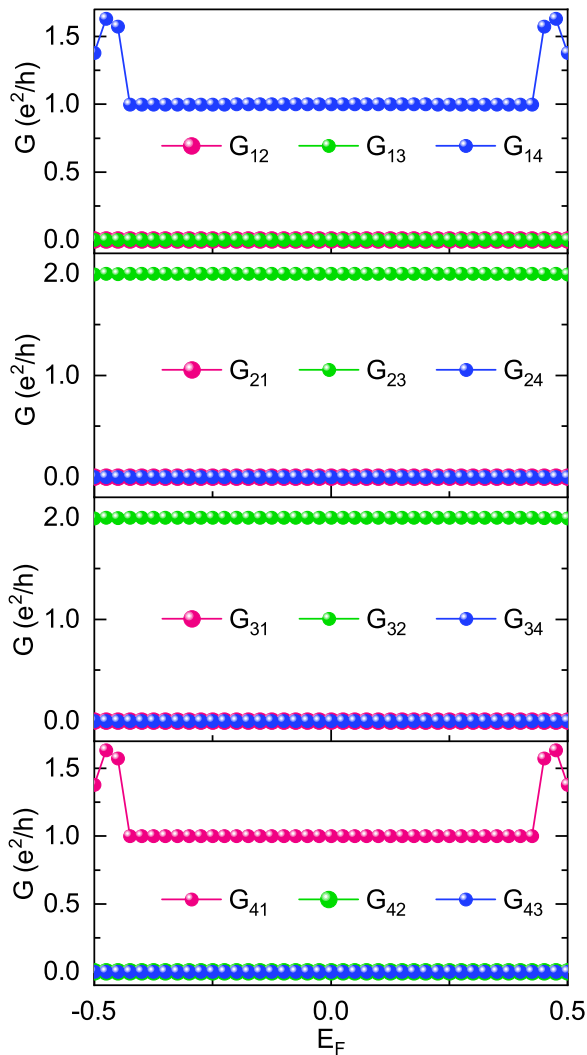


FIG. 12. The four-terminal conductance of the two-region topological junction with $(C_1, C_2) = (1, -2)$ as a function of Fermi level E_F .

Research Funds for the Central Universities (Grants No. WK3510000010 and No. WK2030020032), Anhui Initiative in Quantum Information Technologies (Grant No. AHY170000), and Innovation Program for Quantum Science and Technology (Grant No. 2021ZD0302800). We are grateful to AM-HPC and Supercomputing Center of USTC for providing the high-performance computing resources.

APPENDIX A: ELECTRONIC PROPERTIES OF TOPOLOGICAL JUNCTIONS WITH TWO DOMAINS HARBORING OPPOSITE CHERN NUMBERS

As displayed in Figs. 9(a)–9(b), when $C_1 = -C_2 = 1$, the topological junction is periodic along the x direction, and we can observe the counterpropagating double-degenerated gapless states labeled by red and blue in the one-dimensional band structures. One can see from Fig. 9(c) that the wave-function distributions of the gapless states denoted by the dots in Fig. 9(b) are mainly distributed along the junction

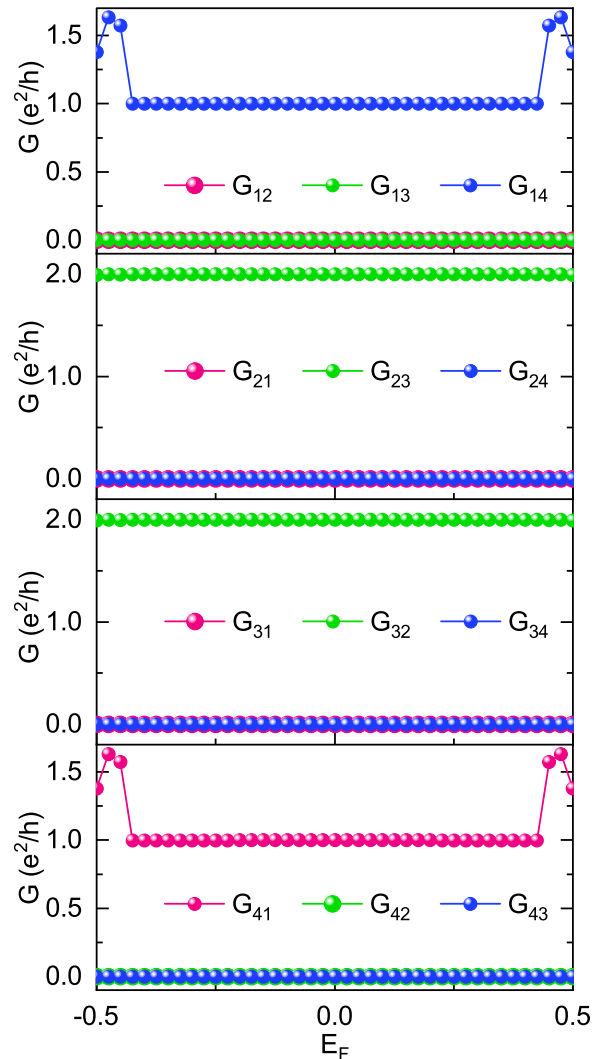


FIG. 13. The four-terminal conductance of the two-region topological junction with $(C_1, C_2) = (-1, 2)$ as a function of Fermi level E_F .

interface for the red gapless states, and along the sample edges for the blue gapless states, as explicitly demonstrated in Fig. 9(a). Similarly, when $C_1 = -C_2 = 2$, as displayed in Figs. 9(d)–9(f), the gapless states are quadruple degenerated and the wave function distributions shown in Fig. 9(f) are similar to those in Fig. 9(c). The explicit gapless states are displayed in Fig. 9(d), where two pairs of edge states propagate along the $-x$ direction and four gapless states propagate along the x direction of the junction interface. Therefore, when $C_1 = -C_2$, the total number of conducting channels along the junction interface is even and equals to $|C_1 - C_2| = 2|C_1|$. Compared with the previous one-dimensional conducting channels in $C = 1$ QAH junctions [26,27], we can now create multiple conducting channels in high-Chern-number topological junctions, which is advantageous for experimental detection due to the advanced technology in fabricating magnetic topological insulators with large Chern number and the larger electronic conductance.

APPENDIX B: FOUR-TERMINAL CONDUCTANCE OF THE TOPOLOGICAL JUNCTIONS WITH TWO DOMAINS

Figures 10–13 display the four-terminal conductances of two-region topological junctions as a function of the

Fermi level. The combinations of the Chern numbers (C_1, C_2) in the two regions are, respectively, (1, 2) for Fig. 10, (−1, −2) for Fig. 11, (1, −2) for Fig. 12, and (−1, 2) for Fig. 13.

-
- [1] F. D. M. Haldane, *Phys. Rev. Lett.* **61**, 2015 (1988).
- [2] C.-X. Liu, S.-C. Zhang, and X.-L. Qi, *Annu. Rev. Condens. Matter Phys.* **7**, 301 (2016).
- [3] Y. Ren, Z. Qiao, and Q. Niu, *Rep. Prog. Phys.* **79**, 066501 (2016).
- [4] K. He, Y. Wang, and Q.-K. Xue, *Annu. Rev. Condens. Matter Phys.* **9**, 329 (2018).
- [5] C.-Z. Chang, C.-X. Liu, and A. H. MacDonald, *Rev. Mod. Phys.* **95**, 011002 (2023).
- [6] D. J. Thouless, M. Kohmoto, M. P. Nightingale, and M. den Nijs, *Phys. Rev. Lett.* **49**, 405 (1982).
- [7] R. Yu, W. Zhang, H.-J. Zhang, S.-C. Zhang, X. Dai, and Z. Fang, *Science* **329**, 61 (2010).
- [8] Z. Qiao, S. A. Yang, W. Feng, W.-K. Tse, J. Ding, Y. Yao, J. Wang, and Q. Niu, *Phys. Rev. B* **82**, 161414(R) (2010).
- [9] Z. F. Wang, Z. Liu, and F. Liu, *Phys. Rev. Lett.* **110**, 196801 (2013).
- [10] S.-C. Wu, G. Shan, and B. Yan, *Phys. Rev. Lett.* **113**, 256401 (2014).
- [11] C. Fang, M. J. Gilbert, and B. A. Bernevig, *Phys. Rev. Lett.* **112**, 046801 (2014).
- [12] Z. Qiao, W. Ren, H. Chen, L. Bellaïche, Z. Zhang, A. H. MacDonald, and Q. Niu, *Phys. Rev. Lett.* **112**, 116404 (2014).
- [13] Q.-Z. Wang, X. Liu, H.-J. Zhang, N. Samarth, S.-C. Zhang, and C.-X. Liu, *Phys. Rev. Lett.* **113**, 147201 (2014).
- [14] G. Xu, B. Lian, and S.-C. Zhang, *Phys. Rev. Lett.* **115**, 186802 (2015).
- [15] S. Qi, Z. Qiao, X. Deng, E. D. Cubuk, H. Chen, W. Zhu, E. Kaxiras, S. B. Zhang, X. Xu, and Z. Zhang, *Phys. Rev. Lett.* **117**, 056804 (2016).
- [16] H. Sun, B. Xia, Z. Chen, Y. Zhang, P. Liu, Q. Yao, H. Tang, Y. Zhao, H. Xu, and Q. Liu, *Phys. Rev. Lett.* **123**, 096401 (2019).
- [17] P. Högl, T. Frank, K. Zollner, D. Kochan, M. Gmitra, and J. Fabian, *Phys. Rev. Lett.* **124**, 136403 (2020).
- [18] T. Devakul and L. Fu, *Phys. Rev. X* **12**, 021031 (2022).
- [19] C.-Z. Chang, J. Zhang, X. Feng, J. Shen, Z. Zhang, M. Guo, K. Li, Y. Ou, P. Wei, L.-L. Wang, Z.-Q. Ji, Y. Feng, S. Ji, X. Chen, J. Jia, X. Dai, Z. Fang, S.-C. Zhang, K. He, Y. Wang *et al.*, *Science* **340**, 167 (2013).
- [20] C.-Z. Chang, W. Zhao, D. Y. Kim, P. Wei, J. K. Jain, C. Liu, M. H. W. Chan, and J. S. Moodera, *Phys. Rev. Lett.* **115**, 057206 (2015).
- [21] C.-Z. Chang, W. Zhao, D. Y. Kim, H. Zhang, B. A. Assaf, D. Heimann, S.-C. Zhang, C. Liu, M. H. W. Chan, and J. S. Moodera, *Nature Mater.* **14**, 473 (2015).
- [22] Y. Deng, Y. Yu, M. Z. Shi, Z. Guo, Z. Xu, J. Wang, X. H. Chen, and Y. Zhang, *Science* **367**, 895 (2020).
- [23] M. Serlin, C. L. Tschirhart, H. Polshyn, Y. Zhang, J. Zhu, K. Watanabe, T. Taniguchi, L. Balents, and A. F. Young, *Science* **367**, 900 (2020).
- [24] T. Li, S. Jiang, B. Shen, Y. Zhang, L. Li, Z. Tao, T. Devakul, K. Watanabe, T. Taniguchi, L. Fu, J. Shan, and K. F. Mak, *Nature (London)* **600**, 641 (2021).
- [25] I. T. Rosen, E. J. Fox, X. Kou, L. Pan, K. L. Wang, and D. Goldhaber-Gordon, *npj Quantum Mater.* **2**, 69 (2017).
- [26] K. Yasuda, M. Mogi, R. Yoshimi, A. Tsukazaki, K. S. Takahashi, M. Kawasaki, F. Kagawa, and Y. Tokura, *Science* **358**, 1311 (2017).
- [27] Y. Ren, J. Zeng, K. Wang, F. Xu, and Z. Qiao, *Phys. Rev. B* **96**, 155445 (2017).
- [28] N. Varnava, J. H. Wilson, J. H. Pixley, and D. Vanderbilt, *Nature Commun.* **12**, 3998 (2021).
- [29] W. Liang, T. Hou, J. Zeng, Z. Liu, Y. Han, and Z. Qiao, *Phys. Rev. B* **107**, 075303 (2023).
- [30] B.-L. Wu, Z.-B. Wang, Z.-Q. Zhang, and H. Jiang, *Phys. Rev. B* **104**, 195416 (2021).
- [31] C. Xiao, J. Tang, P. Zhao, Q. Tong, and W. Yao, *Phys. Rev. B* **102**, 125409 (2020).
- [32] B. Lian, X.-Q. Sun, A. Vaezi, X.-L. Qi, and S.-C. Zhang, *Proc. Natl. Acad. Sci. USA* **115**, 10938 (2018).
- [33] A. A. Burkov and L. Balents, *Phys. Rev. Lett.* **107**, 127205 (2011).
- [34] H. Jiang, Z. Qiao, H. Liu, and Q. Niu, *Phys. Rev. B* **85**, 045445 (2012).
- [35] J. Ge, Y. Liu, J. Li, H. Li, T. Luo, Y. Wu, Y. Xu, and J. Wang, *Natl. Sci. Rev.* **7**, 1280 (2020).
- [36] H. Li, C.-Z. Chen, H. Jiang, and X. C. Xie, *Phys. Rev. Lett.* **127**, 236402 (2021).
- [37] J. Cai, D. Ovchinnikov, Z. Fei, M. He, T. Song, Z. Lin, C. Wang, D. Cobden, J.-H. Chu, Y.-T. Cui, C.-Z. Chang, D. Xiao, J. Yan, and X. Xu, *Nature Commun.* **13**, 1668 (2022).
- [38] Y. Han, S. Sun, S. Qi, X. Xu, and Z. Qiao, *Phys. Rev. B* **103**, 245403 (2021).
- [39] Z. Li, Y. Han, and Z. Qiao, *Phys. Rev. Lett.* **129**, 036801 (2022).
- [40] G. Chen, A. L. Sharpe, E. J. Fox, Y.-H. Zhang, S. Wang, L. Jiang, B. Lyu, H. Li, K. Watanabe, T. Taniguchi, Z. Shi, T. Senthil, D. Goldhaber-Gordon, Y. Zhang, and F. Wang, *Nature (London)* **579**, 56 (2020).
- [41] G. Jiang, Y. Feng, W. Wu, S. Li, Y. Bai, Y. Li, Q. Zhang, L. Gu, X. Feng, D. Zhang, C. Song, L. Wang, W. Li, X. Ma, Q. Xue, Y. Wang, and K. He, *Chin. Phys. Lett.* **35**, 076802 (2018).
- [42] Y.-F. Zhao, R. Zhang, R. Mei, L.-J. Zhou, H. Yi, Y.-Q. Zhang, J. Yu, R. Xiao, K. Wang, N. Samarth, M. H. W. Chan, C.-X. Liu, and C.-Z. Chang, *Nature (London)* **588**, 419 (2020).
- [43] Y.-F. Zhao, R. Zhang, L.-J. Zhou, R. Mei, Z.-J. Yan, M. H. W. Chan, C.-X. Liu, and C.-Z. Chang, *Phys. Rev. Lett.* **128**, 216801 (2022).
- [44] D. Ovchinnikov, J. Cai, Z. Lin, Z. Fei, Z. Liu, Y.-T. Cui, D. H. Cobden, J.-H. Chu, C.-Z. Chang, D. Xiao, J. Yan, and X. Xu, *Nature Commun.* **13**, 5967 (2022).

- [45] Y.-F. Zhao, R. Zhang, J. Cai, D. Zhuo, L.-J. Zhou, Z.-J. Yan, M. H. W. Chan, X. Xu, and C.-Z. Chang, *Nature Commun.* **14**, 770 (2023).
- [46] J. R. Williams, L. DiCarlo, and C. M. Marcus, *Science* **317**, 638 (2007).
- [47] B. Özyilmaz, P. Jarillo-Herrero, D. Efetov, D. A. Abanin, L. S. Levitov, and P. Kim, *Phys. Rev. Lett.* **99**, 166804 (2007).
- [48] L. Fu, C. L. Kane, and E. J. Mele, *Phys. Rev. Lett.* **98**, 106803 (2007).
- [49] S. Datta, *Electronic Transport in Mesoscopic Systems* (Cambridge University Press, Cambridge, 1997).
- [50] M. P. L. Sancho, J. M. L. Sancho, and J. Rubio, *J. Phys. F: Met. Phys.* **14**, 1205 (1984).
- [51] I. Martin, Y. M. Blanter, and A. F. Morpurgo, *Phys. Rev. Lett.* **100**, 036804 (2008).
- [52] G. W. Semenoff, V. Semenoff, and F. Zhou, *Phys. Rev. Lett.* **101**, 087204 (2008).
- [53] Z. Qiao, J. Jung, Q. Niu, and A. H. MacDonald, *Nano Lett.* **11**, 3453 (2011).
- [54] M. Ezawa and N. Nagaosa, *Phys. Rev. B* **88**, 121401(R) (2013).
- [55] Y. Han, S. You, and Z. Qiao, *Phys. Rev. B* **105**, 155301 (2022).